

Retrieval of target structure information from laser-induced photoelectrons by few-cycle bicircular laser fields

Van-Hung Hoang,^{1,2} Van-Hoang Le,² C. D. Lin,¹ and Anh-Thu Le¹

¹*Department of Physics, Cardwell Hall, Kansas State University, Manhattan, Kansas 66506, USA*

²*Department of Physics, Ho Chi Minh City University of Pedagogy, 280 An Duong Vuong Street, District 5, Ho Chi Minh City, Vietnam*

(Received 29 December 2016; revised manuscript received 25 January 2017; published 9 March 2017)

By analyzing theoretical results from a numerical solution of the time-dependent Schrödinger equation for atoms in few-cycle bicircular laser pulses, we show that high-energy photoelectron momentum spectra can be used to extract accurate elastic scattering differential cross sections of the target ion with free electrons. We find that the retrieval range for a scattering angle with bicircular pulses is wider than with linearly polarized pulses, although the retrieval method has to be modified to account for different returning directions of the electron in the continuum. This result can be used to extend the range of applicability of ultrafast imaging techniques such as laser-induced electron diffraction and for the accurate characterization of laser pulses.

DOI: [10.1103/PhysRevA.95.031402](https://doi.org/10.1103/PhysRevA.95.031402)

With the advent of few-cycle intense laser technology, ultrafast imaging techniques such as laser-induced electron diffraction (LIED) [1–12] and high-order harmonic spectroscopy (HHS) [13–19] have recently been proposed. These techniques have been demonstrated to be capable of imaging molecular structural changes with unprecedented subangstrom spatial and few-femtosecond temporal resolutions [10,11,14,19]. Both these techniques are based on the rescattering physics [20,21] with linearly polarized laser pulses.

Quite recently, efficient high-order harmonic generation with bicircular pulses has been achieved [22,23], which provides a new tabletop circularly polarized coherent extreme ultraviolet to soft x-ray source with photon energies up to 160 eV [24]. Subsequently, these harmonics have been demonstrated to be very sensitive to electronic structure [25–31]. Clearly, in a bicircular pulse, after tunneling ionization from the target, the electron in the continuum is driven in a two-dimensional (2D) plane of the laser polarizations, instead of being confined to the laser polarization direction, as in the linearly polarized case. This fact has been utilized by Mancuso *et al.* [32] as a way to decouple the electron tunneling angle from the rescattering angle. Mancuso *et al.* found that this decoupling in turn leads to the separation of rescattered electrons in the low-energy region, in contrast to the linearly polarized case, where they are normally contaminated by the direct electrons.

Previous experimental studies of electron spectra in bicircular laser fields have been mostly limited to the low-energy region so far [32,33]. On the theory side, both low- and high-energy regions have been studied by the strong-field approximation (SFA) [34,35] as well as the classical trajectory Monte Carlo method [33]. However, these works mainly focused on a comparison with experiments at low energies [33] or analyzing the SFA results in terms of the quantum orbit theory [34,35].

In this Rapid Communication, based on the numerical solution of the time-dependent Schrödinger equation (TDSE) for different atoms in few-cycle bicircular laser pulses, we show that high-energy photoelectron spectra can be decoded to reveal the imprints of target structures in the form of accurate elastic scattering differential cross sections (DCSs), although the retrieval method has to be modified as compared to the

linearly polarized lasers. As a consequence of the separation of the electron tunneling angle from the rescattering angle and our ability to steer the continuum in the 2D plane, the accessible range of the “retrievable” scattering angle is shown to increase as compared to the linearly polarized case. Furthermore, our retrieval procedure has also revealed the nature of the electron trajectory driven by the laser pulse in the continuum, which can be potentially used as a method to characterize the laser pulses themselves. We remark that our results can be considered as an extension of the quantitative rescattering theory (QRS) [6,36,37] to the bicircular fields.

For our purpose we solve the TDSE for an atom within the single-active-electron (SAE) approximation with the model potential taken from Ref. [38]. The electron-laser interaction is given in the length gauge as

$$V_L(\mathbf{r}, t) = \mathbf{E}(t)\mathbf{r}. \quad (1)$$

The electric field vector of the bicircular laser fields is chosen to be in the xy plane and has the form

$$\mathbf{E}(t) = \frac{E_0}{\sqrt{2}} \cos^2\left(\frac{\pi t}{nT}\right) [\cos(\omega t)\mathbf{i} + \sin(\omega t)\mathbf{j} + \cos(2\omega t)\mathbf{i} - \sin(2\omega t)\mathbf{j}], \quad (2)$$

with $nT/2 \geq t \geq -nT/2$ and $E(t) = 0$ elsewhere, where $T = 2\pi/\omega$ is the optical period of the fundamental laser. Here, \mathbf{i} and \mathbf{j} are the unit vectors along the x and y axis, respectively. This means that the field consists of a left-handed circularly polarized pulse of the wavelength of $\lambda = 2\pi c/\omega$, with c being the speed of light, and a right-handed circularly polarized pulse wave of the wavelength of $\lambda/2$, both propagating in the same direction along the z axis. All the calculations are done with a four-cycle laser (i.e., $n = 4$) with a wavelength $\lambda = 800$ nm. Unless otherwise indicated, we will use a laser peak intensity of 0.7×10^{14} W/cm² for each of the pulses. The resulting electric field and its vector potential is shown as a Lissajous curve in the xy plane in Figs. 1(a) and 1(b), respectively.

We solve the TDSE by the split-operator method [36] with the ground-state wave function at time $t = 0$ $\Psi(\mathbf{r}, t = 0)$ taken as the initial wave function. For a rare-gas atom, we need to consider degenerate states with $p_{m=0, \pm 1}$. Due to our choice of the coordinate frame with the quantization axis along the

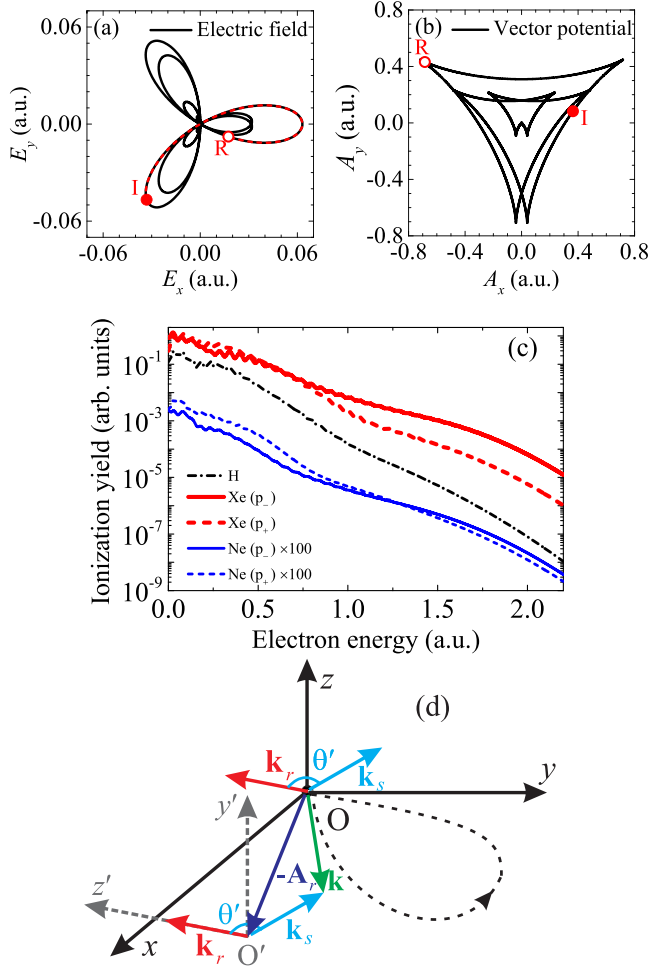


FIG. 1. (a) The electric field (Lissajous curve) of the laser used in the calculations and (b) its vector potential. An ionization (and return) event is marked as I (and R), which gives the return energy near $2.25U_p$. (c) Electron energy spectra from H, Ne, and Xe. Note that the yields for Ne have been multiplied by a factor of 100. (d) Schematic of the kinematics and the notations used in the text. The laser polarizations are in the xy plane. The electron trajectory is shown as a dashed line in the xy plane, with the return momentum \mathbf{k}_r . z' and y' axes of the new frame F' are also shown. See text for details.

z axis, only the initial states with $m = 1$ and $m = -1$ are expected to contribute significantly. Indeed, we have found that the contribution from the initial p_0 state is negligible. Once the final wave function at $t = nT/2$ is obtained, the probability for a photoelectron with momentum \mathbf{k} is calculated by projecting the final wave function onto the scattering states $\Psi_{\mathbf{k}}^-(\mathbf{r})$ as

$$S(\mathbf{k}) = |\langle \Psi(\mathbf{r}, nT/2) | \Psi_{\mathbf{k}}^-(\mathbf{r}) \rangle|^2. \quad (3)$$

The photoelectron energy spectrum is calculated by integrating over all electron emission directions at fixed energies $E = k^2/2$. For our laser parameters, the TDSE is typically solved within a spherical box of a radius up to $R_{\max} = 800$ a.u. with 1600 grid points, with a number of partial waves up to $L_{\max} = 180$ and $m = -L_{\max}$ to L_{\max} , and 1000 time steps per one optical cycle of the fundamental laser field. All

these parameters have been carefully checked to ensure the convergence of the final three-dimensional (3D) momentum distribution.

Electron energy spectra for H, Ne, and Xe are shown in Fig. 1(c). For Ne and Xe we show results from both $m = 1$ and $m = -1$, denoted as p_+ and p_- , respectively. The contributions from $m = 0$ are significantly weaker (not shown). The yields are strongest for Xe and weakest for Ne, as expected on the basis of their ionization potentials. Note that the yields from Ne have been multiplied by a factor of 100. The ponderomotive energy is defined as $U_p = U_{p1} + U_{p2} = 0.19$ a.u., where $U_{pi} = E_0^2/4\omega_i^2$, with $i = 1, 2$. At low energies below about $2U_p = 0.38$ a.u., dominated by direct electrons, the yields from p_+ is stronger than from p_- , as seen more clearly in the Ne case. This fact has been addressed in the context of single-color circularly polarized lasers by Barth and Smirnova [39,40]. Interestingly, this trend might be reversed at high energies, as seen more clearly in Xe [41]. In fact, for Xe the yield from p_- is about an order of magnitude stronger than from p_+ for energies above about 1.3 a.u. This possibility has been discussed before within the SFA by Milosevic [42], who also proposed to use this effect as a possible method to generate attosecond spin-polarized electron pulses. We will show below that the differences in the slopes for H, Ne, and Xe, seen in Fig. 1(c) at high energies, are directly related to differences in the large-angle elastic scattering DCSs of these species and have the same origin as for the linearly polarized case [43].

Due to the lack of cylindrical symmetry, the electron momentum spectra depend explicitly on all three components of the final momentum. For simplicity, we first analyze the 2D momentum spectra in the xy plane (which is perpendicular to the laser propagation direction). The 2D spectra $S(k_x, k_y, k_z=0)$ for H, Ne, and Xe are presented in Figs. 2(a)–2(c), respectively. For Ne and Xe only the results from the p_- state are shown, while the results from the p_+ state look very similar to the p_- case. Note that the low-energy part has been analyzed earlier both experimentally and theoretically [32,33]. In this Rapid Communication we only focus on the high-energy part, which entirely comes from rescattered electrons. For each target a three-lobe structure is seen in the high-energy region. The overall shape of the three-lobe structure is the same for all targets, with each lobe rotated by 120° from one another. This reflects the symmetry of the laser and has been analyzed quite recently within the SFA approach [34,35]. Note that for each target the lobes are not identical since our laser pulse is very short [see Fig. 1(a)]. The most striking fact from Fig. 2 is that each target has different structures at large momenta \mathbf{k} . We will show below that these structures are related to the elastic scattering DCSs of free electrons from each target. Indeed, these structures were found to be largely independent of laser parameters. For comparison, we show in Fig. 2(d) the 2D spectrum from Ne ($2p_-$) with the same 800-nm pulse as used in Fig. 2(b) but a different 400-nm pulse with an intensity of 0.5×10^{14} W/cm² and an ellipticity of 0.9. Indeed, the results at large \mathbf{k} look very similar to Fig. 2(b), apart from the weaker signal due to the weaker 400-nm pulse.

The three-lobe structure can be analyzed in a similar fashion in terms of the QRS as for the two-lobe structure in the linearly polarized case [6,36,37]. Indeed, we will show below that the

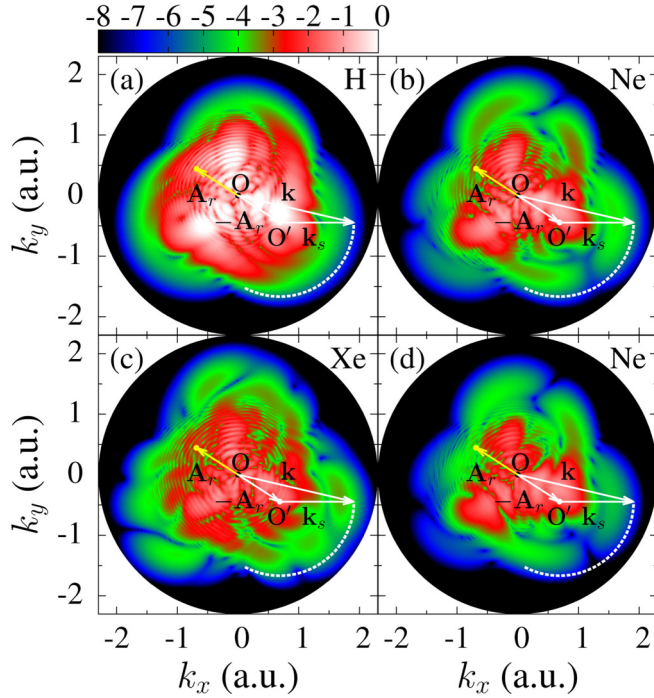


FIG. 2. 2D momentum spectra in the xy plane from H, Ne ($2p_-$), and Xe ($5p_-$) in (a)–(c), respectively. The dashed white circular arcs denote the region where electron yields are extracted in Fig. 3, for $k_s = 1.22$ a.u. (d) Same as (b) but with a different intensity and ellipticity for a 400-nm laser pulse. The peak in each panel has been normalized to 1. See text for details.

high-energy yields in each lobe are directly proportional to the elastic scattering DCS.

Before going into the DCS retrieval procedure, we first discuss the modification from Refs. [6,36,37] due to bicircular laser fields. After tunneling ionization from a target atom, the electron in the continuum can be driven by the laser fields in the 2D xy plane to recollide with the parent ion. The return energy, return direction, and return time t_r depend on the ionization time t_i (i.e., the time when the electron is “born” into the continuum). These parameters can be calculated by solving classical Newton equations or, more accurately, by the quantum orbit theory [35]. A schematic of the kinematics and the notations is given in Fig. 1(d). For illustration we mark in Fig. 1(a) the ionization event (when the electron is “born” into the continuum) and its return to the core that gives a near (classical) maximal return energy of $2.25U_p$. Due to quantum diffusion, higher return energies are also possible. It is important to note that returns with such high energies typically happen at the time when the vector potential is very close to the maximum, as shown in Fig. 1(b). Upon recollision, the electron with momentum \mathbf{k}_r elastically scatters from the parent ion into different directions with momentum \mathbf{k}_s (where $k_r = k_s$) [see the schematic in Fig. 1(d)]. Since the scattering occurs in the laser field, the final momentum is shifted by the vector potential at the moment of rescattering t_r , i.e., by $-\mathbf{A}_r \equiv -\mathbf{A}(t_r)$. In other words, $\mathbf{k} = -\mathbf{A}_r + \mathbf{k}_s$ in the “laboratory” frame F . The nature of this shift is the same as in the linearly polarized case [6,36,37]. For convenience we choose a new frame F' defined with the origin shifted from O by $-\mathbf{A}_r$ to O' , as shown

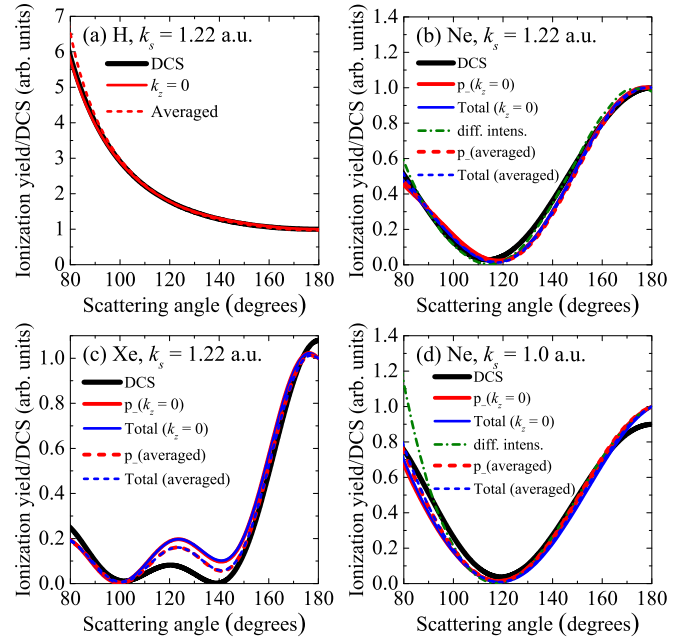


FIG. 3. (a)–(c) Extracted yields along the white arcs shown in Fig. 2 with a “radius” $k_s = 1.22$ a.u., for H, Ne, and Xe, respectively. Different extraction procedures were used (see the labels). The sum of yields from p_- and p_+ is labeled as “total.” Results extracted from Fig. 2(d) are labeled as “diff. intens.” The averaged results from 3D momentum spectra are labeled as “averaged.” (d) Same as (b) but for $k_s = 1.0$ a.u. Note that the blue curves are almost on top of the red curves in all cases. The theoretical laser-free DCS is shown as a thick solid black line. The photoelectron yields have been normalized to that of the DCS near 180° .

in Fig. 1(d), and with the z' axis along the electron return direction, the y' axis parallel to the z axis of the original frame F , and the x' axis (not shown) is in the xy plane. With this choice, the scattering angles θ' and φ' are polar and azimuthal angles of \mathbf{k}_s in frame F' . Note that φ' is defined with respect to the x' axis so that $\varphi' = 0$ corresponds to scattering in the xy plane.

Let us now analyze the 2D momentum image for Ne ($2p_-$) shown in Fig. 2(b). We will focus on the large momenta in the lower right lobe, that is, with the vector potential at the return \mathbf{A}_r being similar to that in Fig. 1(b) (marked as R). According to the analysis above, returning the electron with momentum \mathbf{k}_r , scattered with different scattering angles θ' to a final momentum $\mathbf{k} = -\mathbf{A}_r + \mathbf{k}_s$ (with $k_s = k_r$), shows up as a circular arc, which is presented as a dashed white line in Fig. 2(b). Note that the 2D spectrum in the xy plane corresponds to $\varphi' = 0$ in our convention. This white arc represents backscattered electrons, while the forward-scattered electrons are contaminated by the other $\frac{1}{3}$ subcycles of the laser as well as direct electrons. The yields along this arc for the case of $k_s = 1.22$ a.u., labeled as $p_-(k_z = 0)$ in Fig. 3(b), agree very well with the laser-free elastic scattering DCS. Here, we have normalized the yields to that of the DCS near 180° . Similar good agreements were also found for H and Xe, as shown in Figs. 3(a) and 3(c), respectively, and for Ne at $k_s = 1.0$ a.u., as shown in Fig. 3(d). For Xe, we observed some small discrepancy in the range of $[120^\circ - 140^\circ]$.

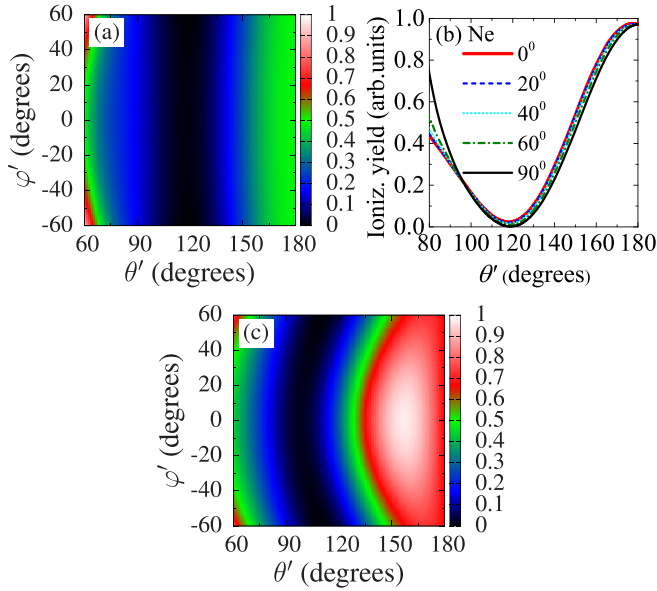


FIG. 4. (a) Yields extracted with a “proper” choice of return direction (or z' axis) with $k_s = 1.22$ a.u. for Ne ($2p_-$) as a function of scattering angles $\{\theta', \varphi'\}$. (b) A few cuts of (a) along different φ' , showing the independence of the “retrieved” DCS on φ' when the proper return direction is used. (c) Same as (a) but with the z' axis rotated by -20° in the xy plane from the proper return direction.

It could be due to the relatively high laser intensity for Xe, which has a quite low ionization potential of 12.1 eV, or it could also be due to slow convergence for the TDSE in the near-saturation regime. We note that the agreements extend down to about 80° , compared to about 100° as in the linearly polarized case with comparable 800-nm lasers [6,36,37]. The extracted yields do not depend much on the laser parameters, except for an overall factor. This fact is illustrated in Figs. 3(b) and 3(d), where the yields extracted from Fig. 2(d) with different laser parameters are also shown (labeled as “diff. intens.”). Indeed, the normalized extracted yields again agree well with the theoretical DCS. These results clearly indicate that the rescattering process in bicircular laser fields can be factorized into a product of a returning electron wave packet and the scattering DCS, as in the QRS theory for a linearly polarized case [6,36,37]. Similarly, the yields from p_+ also agree well with the DCS for Ne and Xe, except for overall factors. These overall factors reflect the differences in the magnitude of the returning wave packets, which in turn depend on ionization rates from the p_- and p_+ of the targets. We also show in Figs. 3(b)–3(d) the total yields resulting from both p_- and p_+ together. They again agree well with the DCS for each case.

So far we have limited the analysis to the 2D momentum spectra in the xy plane. In fact, the white arc in Fig. 2(b) is a cut at $\varphi' = 0$, so each of its points with a fixed θ' can be extended into a circle with φ' that varies from 0° to 360° in 3D momentum space. For convenience, in the following we choose a convention with φ' in the range $\{0, \pm 90^\circ\}$, to better reflect the symmetry of the yields with respect to the change $\varphi' \rightarrow -\varphi'$. With our choice of frame F' , the yields are largely independent of φ' , as illustrated in Fig. 4(a)

for Ne ($2p_-$) with $k_s = 1.22$ a.u. To quantify the level of dependence on φ' , we show in Fig. 4(b) a few cuts at different φ' . The results are indeed nearly indistinguishable, except in the region of $\{\theta' < 90^\circ, \varphi' > 60^\circ\}$. Yields outside this region are contaminated by the data from the direct electrons and the other $\frac{1}{3}$ subcycles. We expect that the contamination region will be reduced with midinfrared lasers, as in the case of linearly polarized lasers. Within the QRS, the independence of yields on φ' is expected since the laser-free DCS depends only on the scattering angle θ' for atomic targets. The origin of the differences in the shapes of ionization yields versus energy from H, Ne, and Xe in Fig. 1(c) can now be understood as due to differences in the DCSs. Indeed, the DCS for H (given by the Rutherford formula) monotonically decreases with energy and scattering angles, while the DCSs for Ne and Xe have structures at large scattering angles, as seen in Figs. 3(b)–3(d), which also depend nonmonotonically on energy. This fact has been analyzed in the case of linearly polarized lasers in Ref. [43].

If the electron return direction (that is, the z' axis) is not accurately determined, the “retrieved” yields would strongly depend on φ' . This situation might occur in real experiments, when the laser parameters are not known accurately so that classical or quantum orbit theory [35] calculations for the return direction are not quite accurate. The result is illustrated in Fig. 4(c) for the case with a wrong electron return direction rotated by -20° in the xy plane from the “exact” one. Clearly, the “extracted” signals would depend on φ' and disagree with the theoretical DCS. This result can therefore be served as a practical method for determining the return direction from the measured 3D data in future experiments. Indeed, the “proper” return direction can be determined as the direction that gives the yields largely independent on φ' for an atomic target, as in Figs. 4(a) and 4(b). Once the proper return direction has been found using this procedure, the extracted yields can also be averaged over a range of $|\varphi'| \leq 60^\circ$. These results are labeled as “averaged” in Fig. 3. They are in general good agreement with the other 2D data described earlier. So far our analysis has been based on a specific choice of the carrier-envelope phase and the time delay between the two laser pulses [see Eq. (2)]. In general, any change in these parameters would lead to a rotation of the three lobes in the momentum spectra around the z axis and a change in the electron return direction for a fixed return energy in each lobe. The method therefore can potentially be used in the future to characterize few-cycle bicircular laser pulses, if the target is known.

In conclusion, we have shown that electron momentum spectra with bicircular laser pulses can be understood within the framework of the quantitative rescattering theory in terms of a product of the returning electron wave packet and the electron-core elastic scattering DCS. Although the results were presented for atomic targets, we expect a similar simplification holds for molecular targets. Thus our results indicate that the LIED technique [9–11] can be extended to bicircular lasers with an added advantage of having a larger range of retrievable scattering angles. The retrievable scattering range can be further extended by using midinfrared lasers. More investigations with longer wavelength lasers would be desirable in the near future as we generally expect the accuracy of the QRS to be improved in the deep tunneling regime.

Using bicircular laser pulses also allows access to different degenerate states that are not accessible with linearly polarized lasers. In this regard, we remark that HHS with bicircular laser pulses has been reported for molecular targets both theoretically [25,29–31] and experimentally [25]. We have also identified a practical method for determining the electron return direction from a 3D momentum image that can be used in future experiments.

V.H.H. and V.H.L. were funded by the Vietnam National Foundation for Science and Technology Development (NAFOSTED) under Grant No. 103.01-2014.44. A.T.L., C.D.L., and V.H.H. were supported in part by the Chemical Sciences, Geosciences and Biosciences Division, Office of Basic Energy Sciences, Office of Science, U.S. Department of Energy under Grant No. DE-FG02-86ER13491, and by the National Science Foundation under Award No. IIA-1430493.

-
- [1] T. Zuo, A. Bandrauk, and P. Corkum, *Chem. Phys. Lett.* **259**, 313 (1996).
- [2] M. Spanner, O. Smirnova, P. B. Corkum, and M. Y. Ivanov, *J. Phys. B* **37**, L243 (2004).
- [3] S. N. Yurchenko, S. Patchkovskii, I. V. Litvinyuk, P. B. Corkum, and G. L. Yudin, *Phys. Rev. Lett.* **93**, 223003 (2004).
- [4] S. X. Hu and L. A. Collins, *Phys. Rev. Lett.* **94**, 073004 (2005).
- [5] M. Meckel, D. Comtois, D. Zeidler, A. Staudte, D. Pavičić, H. C. Bandulet, H. Pépin, J. C. Kieffer, R. Dörner, D. M. Villeneuve, and P. B. Corkum, *Science* **320**, 1478 (2008).
- [6] T. Morishita, A.-T. Le, Z. Chen, and C. D. Lin, *Phys. Rev. Lett.* **100**, 013903 (2008).
- [7] M. Okunishi, T. Morishita, G. Prümper, K. Shimada, C. D. Lin, S. Watanabe, and K. Ueda, *Phys. Rev. Lett.* **100**, 143001 (2008).
- [8] D. Ray, B. Ulrich, I. Bocharova, C. Maharjan, P. Ranitovic, B. Gramkow, M. Magrakvelidze, S. De, I. V. Litvinyuk, A. T. Le, T. Morishita, C. D. Lin, G. G. Paulus, and C. L. Cocke, *Phys. Rev. Lett.* **100**, 143002 (2008).
- [9] J. Xu, Z. Chen, A.-T. Le, and C. D. Lin, *Phys. Rev. A* **82**, 033403 (2010).
- [10] C. I. Blaga, J. Xu, A. D. DiChiara, E. Sistrunk, K. Zhang, P. Agostini, T. A. Miller, L. F. DiMauro, and C. D. Lin, *Nature (London)* **483**, 194 (2012).
- [11] B. Wolter, M. G. Pullen, A.-T. Le, M. Baudisch, K. Doblhoff-Dier, A. Senftleben, M. Hemmer, C. D. Schröter, J. Ullrich, T. Pfeifer, R. Moshhammer, S. Gräfe, O. Vendrell, C. D. Lin, and J. Biegert, *Science* **354**, 308 (2016).
- [12] M. Pullen, B. Wolter, A. T. Le, M. Baudisch, M. Hemmer, A. Senftleben, C. D. Schröter, J. Ullrich, R. Moshhammer, C. D. Lin, and J. Biegert, *Nat. Commun.* **6**, 7262 (2015).
- [13] J. Itatani, J. Levesque, D. Zeidler, H. Niikura, H. Pepin, J. C. Kieffer, P. B. Corkum, and D. M. Villeneuve, *Nature (London)* **432**, 867 (2004).
- [14] S. Baker, J. S. Robinson, C. A. Haworth, H. Teng, R. A. Smith, C. C. Chirilă, M. Lein, J. W. G. Tisch, and J. P. Marangos, *Science* **312**, 424 (2006).
- [15] O. Smirnova, Y. Mairesse, S. Patchkovskii, N. Dudovich, D. Villeneuve, P. Corkum, and M. Y. Ivanov, *Nature (London)* **460**, 972 (2009).
- [16] A.-T. Le, R. R. Lucchese, S. Tonzani, T. Morishita, and C. D. Lin, *Phys. Rev. A* **80**, 013401 (2009).
- [17] S. Haessler, J. Caillat, W. Boutu, C. Giovanetti-Teixeira, T. Ruchon, T. Auguste, Z. Diveki, P. Breger, A. Maquet, B. Carre, R. Taieb, and P. Salieres, *Nat. Phys.* **6**, 200 (2010).
- [18] C. Vozzi, M. Negro, F. Calegari, G. Sansone, M. Nisoli, S. De Silvestri, and S. Stagira, *Nat. Phys.* **7**, 822 (2011).
- [19] P. M. Kraus, B. Mignolet, D. Baykusheva, A. Rupenyan, L. Horný, E. F. Penka, G. Grassi, O. I. Tolstikhin, J. Schneider, F. Jensen, L. B. Madsen, A. D. Bandrauk, F. Remacle, and H. J. Wörner, *Science* **350**, 790 (2015).
- [20] P. B. Corkum, *Phys. Rev. Lett.* **71**, 1994 (1993).
- [21] K. J. Schafer, B. Yang, L. F. DiMauro, and K. C. Kulander, *Phys. Rev. Lett.* **70**, 1599 (1993).
- [22] A. Fleischer, O. Kfir, T. Diskin, P. Sidorenko, and O. Cohen, *Nat. Photon.* **8**, 543 (2014).
- [23] O. Kfir, P. Grychtol, E. Turgut, R. Knut, D. Zusin, D. Popmintchev, T. Popmintchev, H. Nembach, J. M. Shaw, A. Fleischer, H. Kapteyn, M. Murnane, and O. Cohen, *Nat. Photon.* **9**, 99 (2014).
- [24] T. Fan, P. Grychtol, R. Knut, C. Hernandez-Garcia, D. D. Hickstein, D. Zusin, C. Gentry, F. J. Dollar, C. A. Mancuso, C. W. Hogle, O. Kfir, D. Legut, K. Carva, J. L. Ellis, K. M. Dorney, C. Chen, O. G. Shpyrko, E. E. Fullerton, O. Cohen, P. M. Oppeneer, D. B. Milošević, A. Becker, A. A. Jaron-Becker, T. Popmintchev, M. M. Murnane, and H. C. Kapteyn, *Proc. Natl. Acad. Sci. USA* **112**, 14206 (2015).
- [25] D. Baykusheva, M. S. Ahsan, N. Lin, and H. J. Wörner, *Phys. Rev. Lett.* **116**, 123001 (2016).
- [26] L. Medišauskas, J. Wragg, H. van der Hart, and M. Y. Ivanov, *Phys. Rev. Lett.* **115**, 153001 (2015).
- [27] D. B. Milošević, *Phys. Rev. A* **92**, 043827 (2015).
- [28] D. B. Milošević, W. Becker, and R. Kopold, *Phys. Rev. A* **61**, 063403 (2000).
- [29] F. Mauger, A. D. Bandrauk, and T. Uzer, *J. Phys. B* **49**, 10LT01 (2016).
- [30] A. D. Bandrauk, F. Mauger, and K.-J. Yuan, *J. Phys. B* **49**, 23LT01 (2016).
- [31] D. M. Reich and L. B. Madsen, *Phys. Rev. Lett.* **117**, 133902 (2016).
- [32] C. A. Mancuso, D. D. Hickstein, P. Grychtol, R. Knut, O. Kfir, X.-M. Tong, F. Dollar, D. Zusin, M. Gopalakrishnan, C. Gentry, E. Turgut, J. L. Ellis, M.-C. Chen, A. Fleischer, O. Cohen, H. C. Kapteyn, and M. M. Murnane, *Phys. Rev. A* **91**, 031402 (2015).
- [33] C. A. Mancuso, D. D. Hickstein, K. M. Dorney, J. L. Ellis, E. Hasović, R. Knut, P. Grychtol, C. Gentry, M. Gopalakrishnan, D. Zusin, F. J. Dollar, X.-M. Tong, D. B. Milošević, W. Becker, H. C. Kapteyn, and M. M. Murnane, *Phys. Rev. A* **93**, 053406 (2016).
- [34] E. Hasović, W. Becker, and D. B. Milošević, *Opt. Express* **24**, 6413 (2016).
- [35] D. B. Milošević and W. Becker, *Phys. Rev. A* **93**, 063418 (2016).
- [36] Z. Chen, A.-T. Le, T. Morishita, and C. D. Lin, *Phys. Rev. A* **79**, 033409 (2009).
- [37] C. D. Lin, A.-T. Le, Z. Chen, T. Morishita, and R. Lucchese, *J. Phys. B* **43**, 122001 (2010).
- [38] X. M. Tong and C. D. Lin, *J. Phys. B* **38**, 2593 (2005).

- [39] I. Barth and O. Smirnova, *Phys. Rev. A* **84**, 063415 (2011).
- [40] I. Barth and O. Smirnova, *Phys. Rev. A* **87**, 013433 (2013).
- [41] The differences in the high-energy region spectra from $m = 1$ and $m = -1$ states are caused by the interplay of two factors. The first factor is the same as discussed for the low-energy region. The second one is related to the differences in the momentum distribution at the exit of tunneling ionization. For the electron in the continuum to come back to the parent ion and scatter from it, the electron has to appear to the continuum with a finite momentum. A more detailed investigation will be presented elsewhere.
- [42] D. B. Milošević, *Phys. Rev. A* **93**, 051402 (2016).
- [43] Z. Chen, A.-T. Le, T. Morishita, and C. D. Lin, *J. Phys. B* **42**, 061001 (2009).